Scripta Materialia 158 (2019) 24–28

Contents lists available at ScienceDirect

Scripta Materialia

journal homepage: www.elsevier.com/locate/scriptamat

Regular article

Microstructure and tensile property of a novel AlZnMgScZr alloy additively manufactured by gas atomization and laser powder bed fusion

Le Zhou [a,b,*], Hao Pan [c], Holden Hyer [b], Sharon Park [b], Yuanli Bai [c], Brandon McWilliams [d], Kyu Cho [d], Yongho Sohn [a,b]

[a] Advanced Materials Processing and Analysis Center, University of Central Florida, Orlando, FL 32816, USA
[b] Department of Materials Science and Engineering, University of Central Florida, Orlando, FL 32816, USA
[c] Department of Mechanical and Aerospace Engineering, University of Central Florida, Orlando, FL 32816, USA
[d] Weapons and Materials Research Directorate, U.S. Army Research Laboratory, Aberdeen Proving Ground, MD 21005, USA

ARTICLE INFO

Article history:
Received 27 June 2018
Received in revised form 9 August 2018
Accepted 14 August 2018
Available online xxxx

Keywords:
Laser powder bed fusion
Aluminum alloy
Gas atomized powders
Microstructure
Tensile properties

ABSTRACT

Dense and crack-free Al-6Zn-2Mg (wt%) alloys with 1 wt% (Sc + Zr) addition were additively manufactured by laser powder bed fusion (LPBF) using gas atomized powders. As-built microstructure consisted of small equiaxed grains near the melt pool boundary and columnar grains between adjacent melt pools. Alloying of Sc + Zr promoted the formation of Al_3(Sc,Zr) particles, which contributed to the grain refinement. The alloy exhibited outstanding tensile properties (i.e., 418 ± 3 MPa yield strength, 436 ± 3 MPa tensile strength and 11 ± 1% elongation) after heat treatment. The results demonstrate that high strength aluminum alloy can be fabricated by LPBF through alloy design and microstructural control.

Laser powder bed fusion (LPBF) is an innovative technology to manufacture metallic components through a layer by layer process from a powder bed [1]. LPBF has been demonstrated to be applicable to aluminum (Al) alloys, however, mostly limited to Al-Si based alloys that have good castability [2–7]. On the other hand, conventional high strength Al alloys, including 2xxx, 6xxx and 7xxx alloys, are currently difficult to be processed by LPBF. Commonly identified challenges for LPBF of Al alloys include high thermal conductivity, high laser reflectivity and oxide formation. In addition, most high strength Al alloys are susceptible to hot cracking due to high thermal gradient and rapid cooling associated with LPBF [8–11]. As an example, AA7075 alloys have been fabricated by LPBF, and exhibited severe intergranular cracks due to tearing of liquid films between the grains during solidification. [10,12]. Therefore, there is a strong motivation to develop high strength Al alloys that are suitable for LPBF.

Recently, Spierings et al. [13,14], Shi et al. [15] and Yang et al. [16] examined the Al-Mg based alloys with the alloying addition of Sc and Zr. A duplex microstructure that consisted of both columnar and equiaxed grains was obtained. Spierings et al. [13] and Yang et al. [16] suggested that the formation of primary Al_3(Sc,Zr) dispersoids during the solidification facilitated the development of equiaxed grains. Similarly, Croteau et al. [17] reported the potential of Al-Mg-Zr alloys for LPBF applications in which the Al_3Zr formed in the melt during solidification and refined the grains. Martin et al. [12] introduced ZrH_2 nanoparticles to the surface of the AA7075 powders and obtained crack-free LPBF AA7075 alloys. The columnar grain structure was transformed to nearly equiaxed grain structure with the aid of heterogenous nucleation, and thus the crack sensitivity was reduced [12].

In this study, Al-6Zn-2Mg (wt%) alloy was modified with an addition of 1 wt% (Sc + Zr) and processed by LPBF. The addition of 1 wt% (Sc + Zr) was to promote the formation of nucleation particles, and by this to reduce the crack sensitivity of the alloy. Results demonstrate that dense and crack-free AlZnMgScZr alloy can be additively manufactured by LPBF. The microstructure and the tensile properties of this novel alloy are reported and discussed.

Pre-alloyed Al-6Zn-2Mg-1(Sc + Zr) powders were prepared by gas atomization (GA) using a GA system (manufactured by Dong Yang Induction Melting Furnace Co Ltd., Republic of Korea). The nominal composition of the alloy is reported in Table 1. There is impurity element of Fe and Si in the alloy, both of which are <0.1 wt%. The particle size was measured by laser diffraction particle size analyzer (Beckman Coulter LS™ 13 320). The average particle size is 48.8 μm, with a D10, D50 and D90 value of 19.0 μm, 48.1 μm and 77.7 μm, respectively.

A laser powder bed fusion system, SLM® 125^{HL} (SLM solutions, Germany), equipped with a single (400 W) IPG fiber laser with laser beam focus diameter of approximately 100 μm, was employed to

* Corresponding author at: Advanced Materials Processing and Analysis Center, University of Central Florida, Orlando, FL 32816, USA.
E-mail address: le.zhou@ucf.edu (L. Zhou).

https://doi.org/10.1016/j.scriptamat.2018.08.025
1359-6462/

Table 1
Nominal composition of the charge alloys, and XEDS composition of the LPBF alloy in weight percent.

Wt%	Al	Zn	Mg	Sc	Zr
Nominal	Bal.	5.96	2.03	0.68	0.28
LPBF alloy	Bal.	6.04	1.87	0.81	0.23

manufacture the Al-6Zn-2Mg-1(Sc + Zr) alloys. The samples were manufactured with a laser power of 350 W, layer thickness of 30 μm, hatch spacing of 0.13 mm, and scan speed of 900 mm/s. A stripe pattern with a width of 10 mm and a shift between layers was applied. The rotation between adjacent layers was 67°. The temperature of the build plate was kept constant at 100 °C. N_2 was used as protective atmosphere, keeping the O_2 content <0.2% during LPBF build. Cubic samples with a dimension of 12 × 12 × 12 mm were first fabricated for microstructural characterization. A total of 6 tensile bars with a gauge length of 25 mm were manufactured in a horizontal build orientation, following ASTM standards (ASTM E8/E8M). T6 heat treatment with solution heat treatment (SHT) at 480 °C for 1 h, followed by water quenching and artificial aging (AA) at 120 °C for 24 h was carried out to the cubic sample and three of the tensile bars.

Room temperature uniaxial tensile tests were conducted quasi-statically using an MTS universal testing machine. A quasi-static strain rate of 5×10^{-3} mm/s was applied to all tests reported. All deformations were recorded and measured by the Digital Image Correlation (DIC) technique. The system consists of a Tokina AT-X Pro macro 100 mm −f/2.8−d lens with a resolution of 2448 × 2048 and VIC-2D 2009 software by Correlated Solutions, Inc. One DIC camera perpendicular to the specimen plane was used for all tests. The capture frequency was 1 Hz. Engineering stress-strain curves were obtained from MTS machine force with a virtual extensometer through DIC analysis.

The microstructure after polishing and etching was observed by both an optical microscope (Olympus LEXT OLS 3000) and a field emission scanning electron microscope (FE-SEM, Zeiss Ultra-55). X-ray energy dispersive spectroscopy (XEDS) equipped on FE-SEM was employed for compositional analyses. Detailed microstructure was further characterized by a transmission electron microscope (TEM, FEI/Tecnai™ F30 300 kV). In situ lift out (INLO) technique was employed to obtain site-specific TEM thin foils by using a Focused Ion Beam (FIB, FEI TEM200).

The optical microstructure from the XZ cross-section (parallel to build-direction) is presented in Fig. 1(a). Overall, a very small amount of porosity was present, but no cracks were observed. The XZ cross-section exhibited the typical fish-scale patterns along the build direction, which is related to the bottom of the laser melt pool. The area fraction of porosity of the as-built alloy through optical image analysis prior to etching was determined to be <0.4%. Therefore, a near-full density was achieved for the as-built alloy.

Fig. 1(b) and (c) present the backscatter electron (BSE) micrographs from the XZ cross-section of the as-built alloy. Two different grain structures were observed: columnar grains within the melt pool and small equiaxed grains around the melt pool boundary. The columnar grains had widths of a few microns and lengths typically <50 μm, which grew toward the center of the melt pool. On the other hand, the melt pool boundary region exhibited fine equiaxed grains with grain sizes typically in the range between 200 nm to 2 μm. The size of these grains appeared to be slightly coarser than that observed by Spierings et al. [13], which can be attributed to both different alloy composition and LPBF parameters. The microstructure after T6 heat treatment is presented Fig. 1(e) and (f). The as-built microstructure remained after T6 heat treatment, but minor grain growth was observed. Some precipitates were observed along the grain boundaries and were further analyzed by TEM.

Fig. 2(a) presents a high angle annular dark field (HAADF) TEM micrograph from the equiaxed grain region of the as-built alloy. A variety of precipitates/dispersoids showing different contrasts was observed both along the grain boundary and within the grains. Fig. 2(b) shows the results from XEDS mapping from the marked area in Fig. 2(a). Some MgO particles, typically <50 nm in size, were found within the grains. These oxide particles could be from fragmentation of the oxide layer from the powder surface or may form due to oxidation of melt during the LPBF process. Many precipitates that are rich in both Zn and Mg, were observed as white particles in Fig. 2(a). They were determined to be $MgZn_2$, based on the XEDS analysis. Mg_2Si and other Fe-containing dispersoids were also identified, which were typically present adjacent to $MgZn_2$. The Sc-rich precipitates were present both within the grains and along the grain boundary, with a particle size of several tens of nanometers. A selected area diffraction pattern (SADP) from one of the Sc-rich particles within the grains is presented in Fig. 2(c). Despite the strong intensity from the Al grain along the [110] orientation, additional diffraction spots corresponding to the $Al_3(Sc,Zr)$ ($L1_2$) were clearly observed. Based on indexing of Fig. 2(c), the Al_3Sc phase formed a following orientation relationship with the Al matrix: $(001)_{Al} \parallel (001)_{Al_3(Sc,Zr)}$ and $[110]_{Al} \parallel [110]_{Al_3(Sc,Zr)}$.

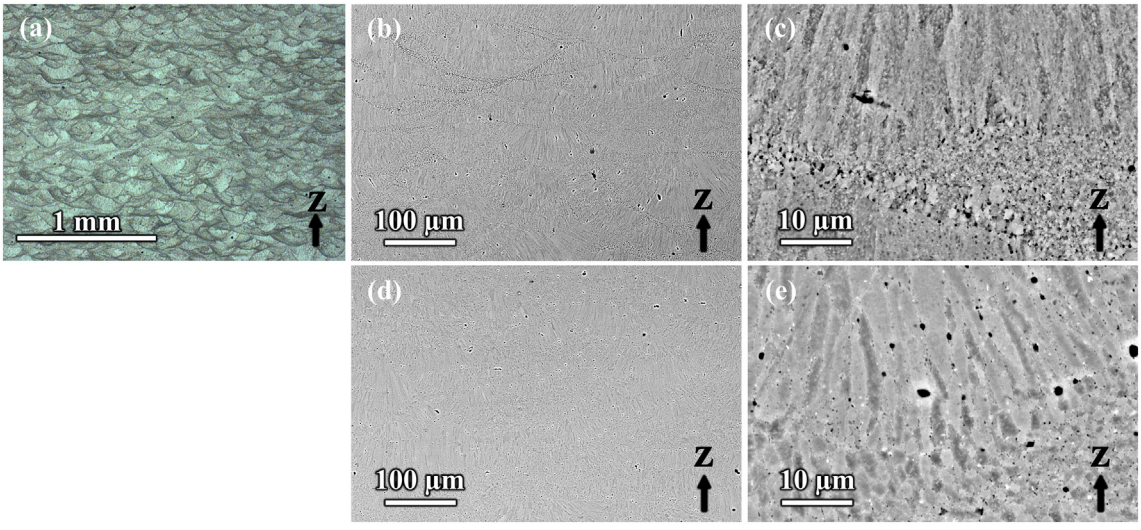

Fig. 1. (a) Optical micrograph of the XZ cross-section from the as-built LPBF AlZnMgScZr alloy. Backscatter electron micrographs of the XZ cross-sections from the LPBF AlZnMgScZr alloy: (b) and (c) as-built, (d) and (e) after T6 heat treatment.

According to the observation from TEM, the $Al_3(Sc,Zr)$ particles appear to be the primary phase formed during solidification [18,19]. These $Al_3(Sc,Zr)$ particles can serve as the heterogeneous nuclei for the Al during solidification and facilitate the formation of equiaxed Al grains. The $Al_3(Sc,Zr)$ particles are coherent with the Al matrix, and thus provide a low energy barrier for the heterogeneous nucleation. For other 7xxx alloys without the alloying of Sc/Zr, LPBF typically resulted in the formation of long columnar grains that extended across several melt pools and solidification cracks along the build direction [12,20]. An epitaxial grain growth might occur where the nucleation is established on previous solidified Al grains, leading to large columnar grains across multiple melt pool boundaries. With the addition of Sc/Zr and thus the formation of $Al_3(Sc,Zr)$ near the melt pool boundary, the formation of new equiaxed grains via heterogeneous nucleation can obstruct the grain growth of the existing grains. As a result, the columnar grains observed in this alloy were much smaller than those observed in LPBF 7xxx alloys without Sc/Zr modification. The refined microstructure with alternating equiaxed grains and columnar grains greatly reduced the crack sensitivity of the alloy. Similar grain refining effects have been observed by Spierings et al. [13,14] and Yang et al. [16] recently in LPBF AlMgScZr alloys.

Since the grain size of the equiaxed grains is much smaller than that of the columnar grains, it is expected that more $Al_3(Sc,Zr)$ nuclei have formed near the melt pool boundary and contributed to the grain refinement. According to Spierings et al. [13], $Al_3(Sc, Zr)$ particles can only survive to approximately 800 °C. Therefore, a large number of $Al_3(Sc, Zr)$ nuclei remained in the mushy zone near the melt pool boundary due to remelting of previous layers [16], where the temperature is lower than 800 °C. On the other hand, the temperature is higher than 800 °C toward the center of the melt pool, hence $Al_3(Sc, Zr)$ particles dissolve into solution. The fast cooling rate associated with the LPBF process results in the formation of supersaturated solid solution by suppressing the formation of $Al_3(Sc,Zr)$ [19,21].

Fig. 3 presents the engineering tensile stress-strain data for the LPBF Al-6Zn-2Mg-1(Sc + Zr) alloy in the as-built state and after T6 heat treatment. A good repeatability was observed for all samples. The corresponding average values of yield stress ($\sigma_{0.2}$), ultimate tensile stress (UTS), elongation at fracture (EL%) and Young's modulus (E) are summarized in Table 2. The stress-strain curves of the as-built samples exhibited a clear strain hardening region after the initial elastic deformation and until the failure occurred. The $\sigma_{0.2}$ and UTS were in the range of 282–285 MPa and 384–387 MPa, respectively, and the EL % reached 18.4%.

The stress-strain data for the LPBF Al-6Zn-2Mg-1(Sc + Zr) alloy after T6 heat treatment exhibited a small plateau region after the elastic deformation, and then strain hardened until the strain reached approximately 8–9%. The strain hardening region is flat compared to that of the as-built alloys. The T6 heat treatment results in an increase of both $\sigma_{0.2}$ and UTS, but a reduction of EL%. After T6 heat treatment, the $\sigma_{0.2}$ and UTS reached 415 to 422 MPa and 432 to 439 MPa, respectively, while the EL% was 10.2 to 12.3%. Fine scale precipitates of ordered and coherent metastable η'-$MgZn_2$ provide strong precipitation hardening to the AlZnMg alloys [22–24]. Apart from the formation of η' precipitates, precipitates of $Al_3(Sc,Zr)$ with $L1_2$ crystal structure will also form

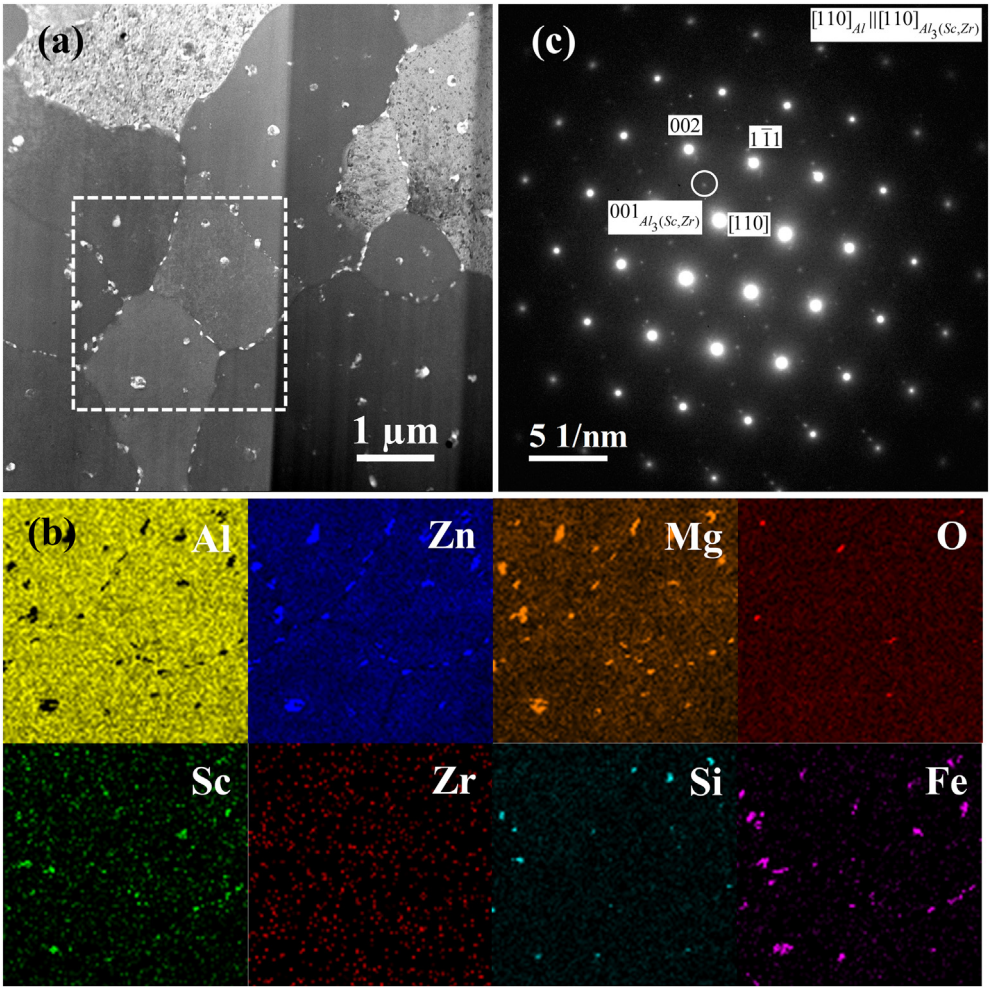

Fig. 2. (a) High angle annular dark field micrograph of the equiaxed grain region of as-built LPBF AlZnMgScZr alloy. (b) XEDS elemental mapping of Al, Zn, Mg, O, Sc, Zr, Si and Fe from marked region in (a). (c) Selected area diffraction pattern of the $Al_3(Sc,Zr)$ particle within the Al grain.

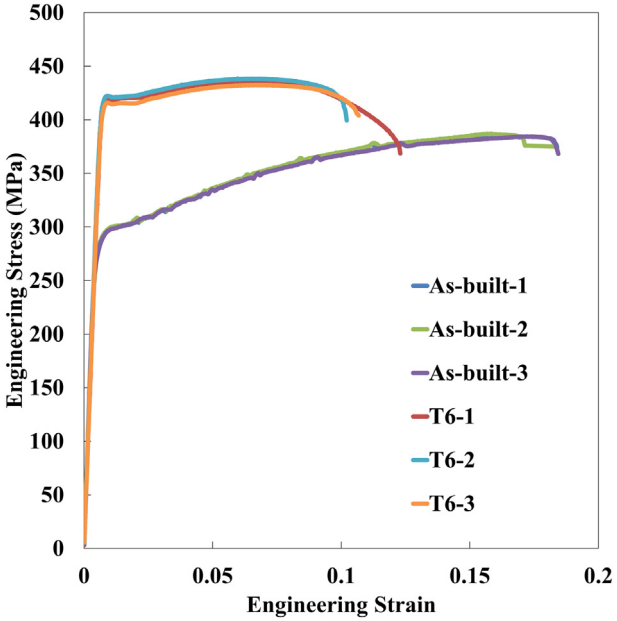

Fig. 3. Engineering stress-strain curves of the LPBF AlZnMgScZr alloys in the as-built state and after T6 heat treatment.

Table 2
Room temperature tensile properties with standard deviations in parenthesis of the LPBF AlZnMgScZr alloys in the as-built state and after T6 heat treatment.

	$\sigma_{0.2}$ (MPa)	UTS (MPa)	EL (%)	E (GPa)
As-built	283.5 (1.5)	386.0 (1.1)	18.4 (0.1)	69.9 (1.7)
T6	418.3 (2.7)	435.7 (2.5)	11.1 (0.9)	65.4 (1.2)

[25,26] in the AlZnMgScZr alloy investigated in this study. Therefore, both η′ and Al_3(Sc,Zr) precipitates are expected to contribute to the strength increase after T6 heat treatment.

The stress-strain curve of the as-built alloys exhibited serrations starting at approximately 2% strain, which can be explained by the Portevin–Le Chatelier (PLC) effect [27]. The PLC effect can be caused by interactions between solute atoms and moving dislocations, which leads to unstable dislocation motion during plastic flow [28]. For the as-built alloy, there is a high concentration of Zn and Mg solutes and a supersaturation of Sc and Zr solutes. When the pinned dislocation by solute atoms moved, a burst in the stress-strain curve is observed. The alloy after T6 exhibited continuous yielding without serrations, due to the formation of precipitates and thus a reduction of solute atoms.

The as-built LPBF AlSi10Mg exhibits a $\sigma_{0.2}$ of 200 to 280 MPa, a UTS of 270 to 470 MPa, and an EL% of 1 to 8% [2–6,29]. After T6 or other heat treatments, the strength of AlSi10Mg alloy can decrease significantly [2–5]. Martin et al. [12]. reported a $\sigma_{0.2}$ of 325 to 373 MPa, a UTS of 383 to 417 MPa, and an EL% of 3.8 to 5.4% for modified (i.e., ZrH_2 coated AA7075 powders) LPBF AA7075 alloys after T6 heat treatment. The alloy, Al-6Zn-2Mg-1(Sc + Zr), examined in this work through gas atomization and LPBF, exhibited higher yield strength and ductility after T6 heat treatment.

The fracture morphologies of the LPBF Al-6Zn-2Mg-1(Sc + Zr) alloy from the as-built and T6 heat-treated samples are presented in Fig. 4. The as-built alloys exhibited non-uniform dimples and some cleavage planes across the fracture surface, as shown in Fig. 4(a) and (b). Occasionally, columnar grains exposed to the fracture surface were observed. This indicates that the fracture mechanism consists of a mix mode of ductile, brittle and intergranular fracture. No apparent necking has been observed for the as-built alloys. The fracture surfaces of the alloys after T6 heat treatment exhibited mostly columnar grain features across the fracture surface and dimples near the regions of equiaxed grain region, as shown in Fig. 4(c) and (d). Therefore, intergranular and ductile fracture are the primary fracture mechanism for the alloys after T6 heat treatment. The intergranular fracture may be related to the formation of precipitates along the grain boundary as shown in Fig. 1(c). All specimens after T6 heat treatment showed clear necking, corresponding to the stress softening in the stress-strain curves in Fig. 3.

Al-6Zn-2Mg-1(Sc + Zr) alloy was additively manufactured by selective laser melting from gas atomized powders with near full density and without cracks. Microstructure consisted of equiaxed grains near the

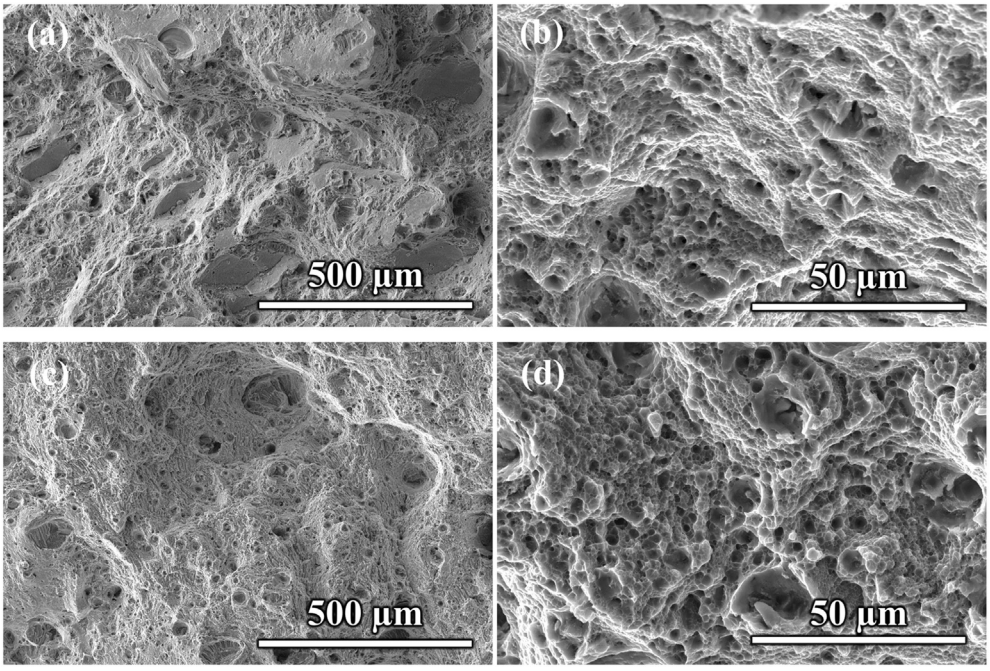

Fig. 4. Secondary electron micrographs of the fracture surfaces of the LPBF AlZnMgScZr alloys: (a) and (b) as-built, (c) and (d) after T6 heat treatment.

melt pool boundary and small columnar grains within the melt pool. TEM demonstrated that coherent $Al_3(Sc,Zr)$ dispersoids formed within the Al grains, and they are expected to serve as heterogeneous nucleation sites for the formation of equiaxed Al grains during solidification. The as-built alloy exhibited engineering yield stress of 284 MPa, ultimate tensile stress of 386 MPa, and elongation of 18.4%. After T6 heat treatment, the LPBF Al-6Zn-2Mg-1(Sc + Zr) alloy exhibited engineering yield stress of 418 MPa, ultimate tensile stress of 436 MPa, and elongation of 11.1%. Microstructural control and alloy design are crucial to the LPBF processing of high strength aluminum alloys.

Acknowledgment

This research was sponsored by the U.S. Army Research Laboratory through cooperative agreement #W911NF-17-2-0172 between University of Central Florida and the U.S. Army Research Laboratory. The views, opinions and conclusions made in this document are those of the authors and should not be interpreted as representing the official policies, either expressed or implied, of the U.S. Army Research Laboratory or the U.S. Government. The U.S. Government is authorized to reproduce and distribute reprints for Government purposes notwithstanding any copyright notation herein.

Appendix A. Supplementary data

Supplementary data to this article can be found online at https://doi.org/10.1016/j.scriptamat.2018.08.025.

References

[1] D. Herzog, V. Seyda, E. Wycisk, C. Emmelmann, Acta Mater. 117 (2016) 371–392.
[2] N. Takata, H. Kodaira, K. Sekizawa, A. Suzuki, M. Kobashi, Mater. Sci. Eng. A 704 (2017) 218–228.
[3] U. Tradowsky, J. White, R. Ward, N. Read, W. Reimers, M. Attallah, Mater. Des. 105 (2016) 212–222.
[4] W. Li, S. Li, J. Liu, A. Zhang, Y. Zhou, Q. Wei, C. Yan, Y. Shi, Mater. Sci. Eng. A 663 (2016) 116–125.
[5] N.T. Aboulkhair, I. Maskery, C. Tuck, I. Ashcroft, N.M. Everitt, Mater. Sci. Eng. A 667 (2016) 139–146.
[6] N. Read, W. Wang, K. Essa, M.M. Attallah, Mater. Des. 65 (2015) (1980–2015) 417–424.
[7] L. Zhou, A. Mehta, E. Schulz, B. McWilliams, K. Cho, Y. Sohn, Mater. Charact. (2018) https://doi.org/10.1016/j.matchar.2018.04.022.
[8] B.A. Fulcher, D.K. Leigh, T.J. Watt, Proc. Solid Freeform Fabrication (SFF) Symposium, 2014.
[9] B. Ahuja, M. Karg, K.Y. Nagulin, M. Schmidt, Phys. Procedia 56 (2014) 135–146.
[10] N. Kaufmann, M. Imran, T. Wischeropp, C. Emmelmann, S. Siddique, F. Walther, Phys. Procedia 83 (2016) 918–926.
[11] P. Skalický, D. Koutný, L. Pantělejev, D. Paloušek, 58th ICMD 2017, 2017.
[12] J.H. Martin, B.D. Yahata, J.M. Hundley, J.A. Mayer, T.A. Schaedler, T.M. Pollock, Nature 549 (7672) (2017) 365.
[13] A. Spierings, K. Dawson, T. Heeling, P. Uggowitzer, R. Schäublin, F. Palm, K. Wegener, Mater. Des. 115 (2017) 52–63.
[14] A.B. Spierings, K. Dawson, M. Voegtlin, F. Palm, P.J. Uggowitzer, CIRP Ann. Manuf. Technol. 65 (1) (2016) 213–216.
[15] Y. Shi, P. Rometsch, K. Yang, F. Palm, X. Wu, Mater. Lett. 196 (2017) 347–350.
[16] K.V. Yang, Y. Shi, F. Palm, X. Wu, P. Rometsch, Scr. Mater. 145 (2018) 113–117.
[17] J.R. Croteau, S. Griffiths, M.D. Rossell, C. Leinenbach, C. Kenel, V. Jansen, D.N. Seidman, D.C. Dunand, N.Q. Vo, Acta Mater. 153 (2018) 35–44.
[18] J. Murray, J. Phase Equilib. 19 (4) (1998) 380.
[19] J. Røyset, N. Ryum, Int. Mater. Rev. 50 (1) (2005) 19–44.
[20] T. Qi, H. Zhu, H. Zhang, J. Yin, L. Ke, X. Zeng, Mater. Des. 135 (2017) 257–266.
[21] K.E. Knipling, D.C. Dunand, D.N. Seidman, Metall. Mater. Trans. A 38 (10) (2007) 2552–2563.
[22] X. Li, V. Hansen, J. Gjønnes, L. Wallenberg, Acta Mater. 47 (9) (1999) 2651–2659.
[23] T. Engdahl, V. Hansen, P. Warren, K. Stiller, Mater. Sci. Eng. A 327 (1) (2002) 59–64.
[24] J. Liu, J. Chen, X. Yang, S. Ren, C. Wu, H. Xu, J. Zou, Scr. Mater. 63 (11) (2010) 1061–1064.
[25] D.N. Seidman, E.A. Marquis, D.C. Dunand, Acta Mater. 50 (16) (2002) 4021–4035.
[26] O. Senkov, M. Shagiev, S. Senkova, D. Miracle, Acta Mater. 56 (15) (2008) 3723–3738.
[27] A. Le Chatelier, Rev. Metall. 6 (8) (1909) 914–917.
[28] A. Yilmaz, Sci. Technol. Adv. Mater. 12 (6) (2011) 063001.
[29] L. Hitzler, C. Janousch, J. Schanz, M. Merkel, B. Heine, F. Mack, W. Hall, A. Öchsner, J. Mater. Process. Technol. 243 (2017) 48–61.